Available online at www.sciencedirect.com
ScienceDirect
Geochimica et Cosmochimica Acta 71 (2007) 1883–1897
Geochimica et Cosmochimica Acta
www.elsevier.com/locate/gca

Bridging arsenate surface complexes on the hematite (0 1 2) surface ☆

Jeffrey G. Catalano [a,*], Zhan Zhang [a], Changyong Park [a], Paul Fenter [a], Michael J. Bedzyk [b,c]

[a] *Chemistry Division, Argonne National Laboratory, Argonne, IL 60439, USA*
[b] *Northwestern University, Evanston, IL 60208, USA*
[c] *Materials Science Divison, Argonne National Laboratory, Argonne, IL 60439, USA*

Received 6 July 2006; accepted in revised form 17 January 2007; available online 21 January 2007

Abstract

The fate of the oxoanion arsenate in diverse systems is strongly affected by its adsorption on the surfaces of iron (oxyhydr)oxide minerals. Predicting this behavior in the environment requires an understanding of the mechanisms of arsenate adsorption. In this study, the binding site and adsorption geometry of arsenate on the hematite (0 1 2) surface is investigated. The structure and termination of the hematite (0 1 2)-water interface were determined by high resolution X-ray reflectivity, revealing that two distinct terminations exist in a roughly 3:1 proportion. The occurrence of multiple terminations appears to be a result of sample preparation, and is not intrinsic to the hematite (0 1 2) surface. X-ray standing wave (XSW) measurements were used to determine the registry of adsorbed arsenate to the hematite structure, and thus the binding site and geometry of the resulting surface complex. Arsenate forms a bridging bidentate complex on two adjacent singly coordinated oxygen groups on each of the two distinct terminations present at the hematite surface. Although this geometry is consistent with that seen in past studies, the derived As–Fe distances are longer, the result of the topology of the FeO_6 octahedra on the (0 1 2) surface. As EXAFS-derived As–Fe distances are often used to determine the adsorption mechanism in environmental samples (e.g., mine tailings, contaminated sediments), this demonstrates the importance of considering the possible sorbent surface structures and arrangements of adsorbates when interpreting such data.

As multiple functional groups are present and multiple binding geometries are possible on the hematite (0 1 2) surface, the XSW data suggest that formation of bridging bidentate surface complexes on singly coordinated oxygen sites is the preferred adsorption mechanism on this and most other hematite surfaces (provided those surfaces contain adjacent singly coordinated oxygen groups). These measurements also constrain the likely reaction stoichiometry, with only the protonation state of the surface complex undetermined. Although bridging bidentate inner-sphere surface complexes comprised the majority of the adsorbed arsenate present on the hematite (0 1 2) surface, there is an additional population of sorbed arsenate species that could not be characterized by the XSW measurements. These species are likely more disordered, and thus more weakly bound, than the bridging bidentate complexes, and may play a role in determining the fate, transport, and bioavailability of arsenate in the environment. Finally, the possibility of obtaining species-specific XSW measurements by tuning the incident beam energy to specific features in a XANES spectrum is described.

* Corresponding author. Fax: +1 630 252 9570.
E-mail address: catalano@anl.gov (J.G. Catalano).

0016-7037/$ - see front matter © 2007 Published by Elsevier Ltd.
doi:10.1016/j.gca.2007.01.015

1. INTRODUCTION

The adsorption of arsenate ($H_nAsO_4^{3-n}$) on mineral surfaces affects its fate, transport, and bioavailability in natural waters. Arsenate-sorbed iron (oxyhydr)oxides are thought to be the source of widespread contamination of shallow groundwater with arsenic in the Bengal Delta region (e.g., Smedley and Kinniburgh, 2002; Polizzotto et al., 2005). The release of arsenic from tailings piles and its transport in acid mine drainage is affected by adsorption/desorption onto iron-bearing phases (e.g., Foster et al., 1998; Savage et al., 2000; Carlson et al., 2002; Courtin-Nomade et al., 2003, 2005; Donahue and Hendry, 2003; Fukushi et al., 2003; Moldovan et al., 2003; Morin et al., 2003; Paktunc et al., 2003, 2004; Beaulieu and Savage, 2005; Walker et al., 2005). Arsenic concentrations in marine and lacustrine systems is often controlled, at least partially, by adsorption onto iron (oxyhydr)oxides (e.g., Devitre et al., 1991; Azcue and Nriagu, 1993; Pichler and Veizer, 1999; Linge and Oldham, 2004). One of the commonly-suggested methods of removal of arsenic from water supplies is through filtration based on adsorption by iron oxides (e.g., Katsoyiannis and Zouboulis, 2002; Thirunavukkarasu et al., 2003; Garelick et al., 2005; Jessen et al., 2005). Understanding the molecular mechanisms of arsenate adsorption is necessary for predicting the long-term fate of arsenic in the environment and for generalizing arsenate adsorption behavior in diverse systems.

Arsenate has been observed to adsorb onto iron (oxyhydr)oxide minerals through an inner-sphere binding mechanism (Goldberg, 1986; Grossl and Sparks, 1995; Grossl et al., 1997; Jain et al., 1999). Past extended X-ray absorption fine structure (EXAFS) spectroscopy studies have attempted to identify the molecular geometry of adsorbed arsenate (e.g., Waychunas et al., 1993, 1995; Manceau, 1995; Fendorf et al., 1997; Sherman and Randall, 2003), suggesting plausible models based on As–Fe interatomic distances, with most studies identifying primarily bridging bidentate complexes. However, none of these studies had the ability to directly determine the registry of the adsorbed As with the structure of the sorbent. A recent study presented X-ray crystal truncation rod (CTR) scattering measurements (from which this registry may be determined) of arsenate adsorption on hematite (0 0 1) and (0 1 2) surfaces, showing changes in the CTR data between the clean and As-sorbed surfaces, confirming that As adsorbs on ordered surface sites (Waychunas et al., 2005a). However, these measurements were made ex situ, and the actual As adsorption sites on these surfaces were not determined by CTR scattering, being only inferred from analysis of complimentary grazing incidence-EXAFS (GI-EXAFS) data.

In this study, we present X-ray reflectivity measurements of the hematite (0 1 2) surface termination and structure, and in situ Bragg-reflection X-ray standing wave (XSW) measurements of arsenate adsorbed inner-sphere on the hematite (0 1 2) surface [Note that the hexagonal (0 1 2) Miller indexed surface is equivalent to the $(01\bar{1}2)$ surface in Bravais-Miller notation, which by 3-fold symmetry is equivalent to the $(1\bar{1}02)$ surface often referenced in the literature.]. The X-ray reflectivity results reveal two distinct, coexisting terminations for the hematite (0 1 2) surface. The relationship of adsorbed As to the hematite crystal structure is visualized through direct inversion of the XSW data using the model-independent XSW imaging approach (Cheng et al., 2003; Okasinski et al., 2004; Zhang et al., 2004), revealing similar sites on the two hematite terminations, and with similar fractional occupancies. The dominant site of adsorbed arsenate is then refined through model-dependent least-squares fitting [often called XSW triangulation (Golovchenko et al., 1982)] using the XSW imaging results as an initial structural model. These results identify the preferred binding site and adsorption geometry on the hematite (0 1 2) surface, and constrain the likely reaction stoichiometry. Finally, the prospects for future XSW studies that are sensitive to registering the adsorption site of chemically distinct species [e.g., As(III) versus As(V)] are discussed.

The hematite (0 1 2) surface was chosen for this study because it is one of the natural growth faces of hematite (Cornell and Schwertmann, 2003), is predicted to be the most energetically stable surface of hematite (Mackrodt et al., 1987; Hartman, 1989), has oxygen functional groups in multiple coordination states (Tanwar et al., 2007), and high-quality hematite crystals with this orientation are commercially available. Investigating arsenate adsorption on this surface, and single crystal surfaces in general, provides fundamental information on the mechanisms of adsorption reactions and the arrangement(s) of an adsorbate with respect to the sorbent crystal structure. This helps constrain and test the assumptions of surface complexation models and demonstrates the types of surface complexes to expect on more complex mineral sorbents. The hematite (0 1 2) surface is an excellent model system for studying reactions on iron (oxyhydr)oxides as it has adjacent (2.89 Å separation) singly coordinated oxygen functional groups, thought to be the most reactive sites for adsorption on iron and aluminum (oxyhydr)oxides surface (e.g., Hiemstra and Van Riemsdijk, 1996, 1999; Venema et al., 1997; Catalano et al., 2006a,b), that are sterically fully accessible (i.e., other nearby surface functional groups will not block adsorbates from reacting with the singly coordinated oxygen sites). Implicit in this is the assumption that singly coordinated oxygen functional groups on various iron (oxyhydr)oxide phases have, to a first approximation, similar reactivity towards adsorbates if sterically unhindered.

2. MATERIALS AND METHODS

2.1. Sample preparation

A natural hematite (α-Fe_2O_3) single crystal was oriented, cut, and polished parallel to (0 1 2) (Tanwar et al., 2007). The crystal was cleaned following previously described procedures (Catalano et al., 2006a,b). Briefly, the sample was rinsed in HPLC-grade acetone and methanol, followed by repeated washing in deionized water (>18 MΩ cm), drying in a stream of Ar gas, and then baking for 3 h at ~350 °C. For the XSW measurements, a solution of 100 μM $Na_2HAsO_4{\cdot}7H_2O$ in 10 mM NaCl was prepared from reagent grade chemicals and deionized water; the pH was adjusted to five with HCl.

2.2. X-ray reflectivity measurements and analysis

To characterize the clean sample surface, high resolution specular X-ray reflectivity data were collected at beamline 12-BM (BESSRC/XOR) at the Advanced Photon Source (APS), Argonne National Laboratory (ANL) (Beno et al., 2001a). The hematite sample was mounted in deionized water in a thin film cell sealed with 8 μm Kapton™ film on a four-circle diffractometer. A Si (1 1 1) monochromator was used to select an incident X-ray wavelength of 0.775 Å (16.0 keV). A double mirror system was employed, with the first mirror, a flat Pd-coated glass ceramic mirror, for harmonic rejection and the second, a toroidal Rh-coated silica mirror, for focusing. The reflected X-ray intensity at each Q value was measured with a CCD area detector. The application of a CCD area detector to the measurement of X-ray reflectivity, including data collection, data integration, and determination of statistical errors, has been described previously (Fenter et al., 2006).

A description of the equations and parameters used in calculations and fitting the experimental data have been described previously (Catalano et al., 2006a). A structural model of the hematite (0 1 2)-water interface was refined through least-squares fitting. Due to the limited resolution of the dataset ($\pi/Q_{max} = 0.75$ Å), atomic positions in each layer could not be refined independently as this results in significant correlations. The structural model consisted of three Fe_2O_3 layers that were allowed to relax (see example layer in Fig. 1). In each layer, the lowest (highest) O atoms were constrained to have the same relaxations as the lowest (highest) Fe atoms. The relaxations of the middle O atoms in the Fe_2O_3 layers were constrained to equal the mean relaxation of the two Fe atoms in each layer. In the uppermost Fe_2O_3 layer, the upper Fe site was left vacant in the final analysis, the upper O site was allowed to relax freely, and the middle O site was constrained to have the same relaxation as the lower Fe site. The electron density profile derived from this refinement includes a spatial broadening term due to the finite resolution of the data (Fenter, 2002). The bulk crystal structure and vibrational amplitudes were taken from Finger and Hazen (1980). The spacing of the Fe_2O_3 layers (Fig. 1) in the bulk structure, corresponding to the d-spacing of the (0 1 2) plane, was measured experimentally to be 3.684 Å, as compared to the value of 3.682 Å of Finger and Hazen (1980). The structural models used to generate the X-ray reflectivity profiles calculated for the ideal full- and half-layer terminations (discussed below) included featureless bulk water starting 2.8 Å above the terminal oxygen planes [i.e., twice the van der Waals radius of oxygen (Pauling, 1960)]. The goodness-of-fit parameter, χ^2, used in the data analysis has been described previously (Geissbuhler et al., 2004). The errors reported for the fitting results are based on the standard deviations obtained from the least squares refinement of the surface structure. All reported errors are at the 95% (2σ) confidence level.

2.3. X-ray standing wave measurements and analysis

XSW measurements were performed in a vertical scattering geometry on a four-circle diffractometer at beamline 12-ID-D (BESSRC/XOR) at the APS (Beno et al., 2001b). The incident X-ray energy (12.102 keV) was selected using a liquid-N_2-cooled, symmetrical Si (1 1 1) monochromator; the beam dispersion was further controlled using two sets of Si (1 1 1) or (2 2 0) double-bounce, channel cut postmonochromators. Entrance slits after the postmonochromators reduced the incident beam size to 0.01 mm^2 in order to illuminate a single grain in the hematite crystal. This allows for analysis of the XSW data using dynamical diffraction theory for "perfect" single crystals. The hematite (0 1 2) single crystal was mounted in deionized water in a sample cell sealed with 8 μm Kapton™ film. After mounting the sample on the diffractometer, approximately 5 mL of the reaction solution were exchanged into and flushed through the cell, and allowed to react for 10 min. The bulk of the solution was then drained from the cell, leaving a thin solution film between the crystal surface and the Kapton™ film [estimated to be ~2 μm thick based on past studies (Bedzyk et al., 1990)]. This cycle was repeated for approximately one hour, after which the cell was sealed and the XSW measurements began. All measurements were made in situ

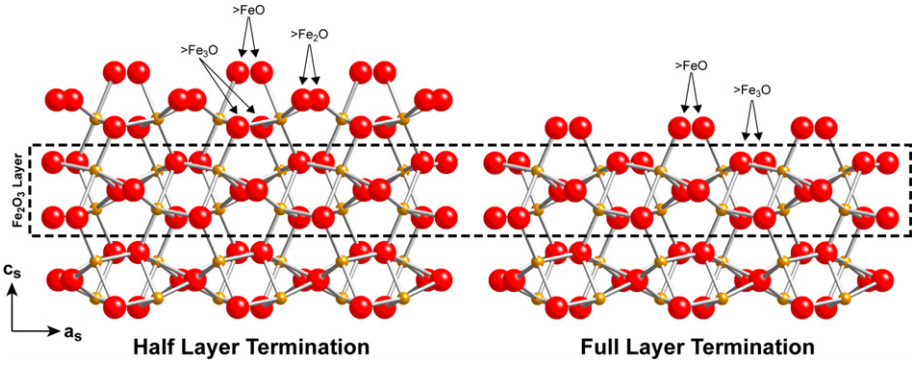

Fig. 1. Structural models of two possible terminations of the α-Fe_2O_3 (0 1 2) surface in aqueous solution. The small spheres are Fe and the large spheres are O; H atoms were not included in the models as their positions cannot be determined by X-ray scattering. Also shown are the sites of important surface functional groups (surface oxygens undercoordinated with respect to bulk oxygens). Although not shown for clarity, it is assumed that these groups protonate and/or hydrogen bond to interfacial water molecules to maintain charge balance and preserve appropriate bond valence sums.

in approximately 24 h. Fe and As Kα X-ray fluorescence were measured using a single-element energy dispersive Ge detector mounted horizontally facing the polarization direction of the incident X-ray beam. The surface coverage of As was measured by comparison of the As Kα X-ray fluorescence from the sample with the Zn Kα X-ray fluorescence from a standard of known Zn coverage; corrections were made for differences in X-ray absorption cross section, fluorescence yield, and linear attenuation. Surface XANES spectra were measured with the postmonochromators removed.

Details of XSW measurements and the determination of adsorbate positions on mineral surfaces can be found in Bedzyk and Cheng (2002). Briefly, the reflectivity, $R(\theta)$, and the X-ray fluorescence yields, $Y(\theta)$, were measured simultaneously by rocking the hematite crystal through the specified $H = hkl$ Bragg reflection from the low-angle to the high-angle side. The resulting modulation of $Y(\theta)$ for the element of interest provides information on the location of the atom with respect to the diffracting plane. For an adsorbate, this modulation takes the form:

$$Y(\theta) = Y_{OB}[1 + R(\theta) + 2\sqrt{R(\theta)}f_H \cos(v(\theta) - 2\pi P_H)], \quad (1)$$

where Y_{OB} is the fluorescence yield at an off-Bragg angle, $v(\theta)$ is the relative phase of the standing wave field, and H is the diffraction vector. The coherent position, P_H, is related to the fractional position of the adsorbate ion with respect to the diffracting plane, and the coherent fraction, f_H, is a measure of the spatial spread of the distribution of the fluorescing ions. $f_H = Ca_H D_H$ consists of three factors: C, the ordered fraction of the fluorescing element; a_H, a geometric factor that accounts for multiple element positions; and D_H, the Debye–Waller factor (Bedzyk and Materlik, 1985a). Model independent parameters P_H and f_H are obtained through fitting Eq. (1) to the experimental $Y(\theta)$.

In addition to monitoring the fluorescence yield of the surface adsorbate, we also (whenever possible) monitor the fluorescence yield of a bulk lattice cation. Since we know the lattice positions of the bulk atoms, this can then be used as a systematic check of our XSW experiment. For the analysis of this bulk X-ray fluorescence yield, Eq. (1) needs to be multiplied by an extinction-effect factor (Batterman, 1964; Bedzyk and Materlik, 1985a). As noted previously (Catalano et al., 2006b), the Fe fluorescent modulations from non-specular reflections were dominated by strong extinction effects (observed as an overall reduction in fluorescent intensity near the Bragg condition) that resulted from using a large take-off angle between the detector and the crystal surface. As a result, these measurements were not sensitive to P_H since the Fe Kα escape depth was much larger than the extinction depth. Instead, the Fe coherent positions for the non-specular reflections were fixed to their crystallographic values in the analysis, which included the effect of extinction.

The XSW-determined parameters P_H and f_H are also the phase and amplitude of the Hth Fourier coefficient of the element-specific normalized density profile (Bedzyk and Materlik, 1985b; Hertel et al., 1985). As recently demonstrated, a measured set of these Fourier coefficients can be Fourier inverted into an element-specific three-dimensional atomic density map in a process called XSW imaging (Okasinski et al., 2004; Zhang et al., 2004). . This method obtains the three-dimensional distribution of the element of interest in a model-independent manner, but with only 0.5–2 Å spatial resolution, depending on the d-spacings of the measured Bragg reflections. The As position with respect to the hematite lattice was further refined using triangulation by least-squares fitting of the atomic coordinates and ordered fraction, C, of As as described previously (Golovchenko et al., 1982). Differences between the model-optimized f_{opt} and P_{opt} and the experimental f_H and P_H values were minimized using least-squares fitting techniques. A fixed isotropic vibrational amplitude of 0.1 Å was used to estimate the Debye–Waller factors, D_H, of As. Errors reported for the triangulation fitting results are based on the standard deviations obtained from the least-squares fitting results. The error on the total surface coverage is derived from counting statistics, and error on the coherent coverage was calculated by propagating the errors from the total surface coverage and the ordered fraction. The uncertainties in the bond length calculations originate from propagating the errors on the triangulation-derived As positions. All reported errors are at the 95% (2σ) confidence level.

3. RESULTS AND DISCUSSION

3.1. Hematite (0 1 2) surface structure

Hematite (α-Fe_2O_3) consists of a distorted hcp oxygen lattice with two-thirds of the octahedral voids occupied by Fe(III). The space group is trigonal ($R\bar{3}c$) with lattice parameters $a = 5.035$ Å, $c = 13.747$ Å, and $\gamma = 120°$ (Finger and Hazen, 1980). In this manuscript, the *hkl* notation is used for bulk indices instead of the full *hkil* notation, as the relationship $h + k + i = 0$ makes the full notation unnecessary. The crystal structure was reindexed using a rectangular surface unit cell with the c-axis normal to the (0 1 2) surface using the method described by Trainor et al. (2002). This reindexing allows for easier visualization of surface structure and determination of the reflections that are symmetry equivalent with respect to the bulk but nonequivalent with respect to the (0 1 2) surface. It should be noted that this surface indexing lacks a rational repeat along the surface normal, which results in some bulk Bragg reflection having non-integer indices in the surface notation. The resulting rectangular surface unit cell is bound by the bulk crystallographic vectors parallel to [−100], [−1/3 −2/3 1/3], and [0.713 1.426 0.287] and can be defined with surface lattice parameters $|a_s| = 5.035$ Å, $|b_s| = 5.427$ Å, $|c_s| = 7.364$ Å. Reflections listed in this surface indexing are labeled with a subscript s.

Assuming all Fe atoms remain sixfold coordinated by O atoms (or OH or H_2O molecules), then there are two crystallographically and chemically distinct terminations of the hematite (0 1 2) surface possible under aqueous conditions (Fig. 1). The first termination consists of a stoichiometric Fe_2O_3 layer with the upper Fe site vacant (half-layer termination). The second possible termination consists of a stoi-

chiometric Fe_2O_3 layer with an additional O layer that completes the coordination shell of the upper Fe site (full-layer termination). While both terminations contain zigzag rows of singly coordinated terminal oxygens (>FeO) along b_s, they differ in that the half-layer termination contains both doubly (>Fe_2O) and triply coordinated (>Fe_3O) oxygen groups, whereas the full-layer termination contains only >Fe_3O groups. Comparison of the calculated reflectivity profiles for these two ideal terminations to the X-ray reflectivity of the sample used in this study reveals that neither of the unrelaxed structures matches the experimental data (Fig. 2a and b). This is not surprising since the calculated reflectivity profiles did not take into account structural relaxations and ordering of interfacial water. However, the shape of the calculated reflectivity profiles (especially the relatively lower reflectivity near $Q = 1$ Å^{-1} compared to $Q = 2.5$ Å^{-1}) was more similar to that expected for a half-layer termination, suggesting that this is the more likely termination.

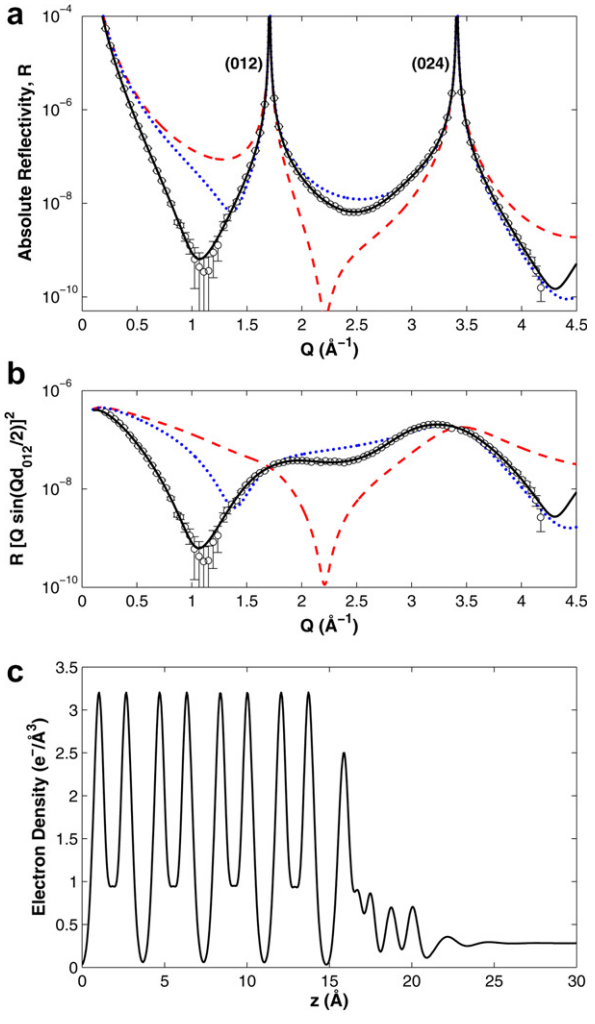

Fig. 2. Absolute (a) and normalized (b) X-ray reflectivity data (circles) and the reflectivity calculated for a full-layer termination (dashed), half-layer termination (dotted), and for the best-fit model (line). (c) Electron density profile of the best-fit structure of the α-Fe_2O_3 (0 1 2)-water interface.

A model that accounts for the important interfacial structural details of this surface was fit to the data using a least-squares refinement. Preliminary fits could not reproduce the measured reflectivity when a fully occupied half-layer termination was assumed ($\chi^2 = 42.06$), and resulted in unrealistic atomic relaxations (fit not shown). Allowing the occupancy of Fe in the terminal layer to relax to 0.75 ± 0.03 resulted in a substantial improvement in the fit quality ($\chi^2 = 1.32$) and excellent reproduction of the measured X-ray reflectivity over the full range of data (Fig. 2). The resulting atomic relaxations (Table 1) were reasonable and the positions of adsorbed and layered water were similar to that recently seen for the α-Al_2O_3 (0 1 2) surface (Catalano et al., 2006a). A lower limit on the lateral surface domain size is $L_\parallel > 4\pi/Q\delta_{2\theta}$ (Fenter, 2002), where $\delta_{2\theta}$ is the angular width of the reflected beam. At $Q = 0.81$ Å^{-1} (the first midzone), $\delta_{2\theta} = 0.138°$ (0.0024 rad), corresponding to $L_\parallel > \sim 6500$ Å.

The reduction in the Fe site occupancy suggests that the hematite (0 1 2) surface has a mixture of half-layer (~75%)

Table 1
Optimized structural parameters from best fit model of the α-Fe_2O_3 (0 1 2)-water interface

Surface structure				
Atom	z_{init}[a] (Å)	z[b] (Å)	σ[c] (Å)	θ[d]
O (H_2O_{ads})[e]		20.05(8)[f]	0.20(3)	1
O (H_2O_{ads})		18.8(1)	0.20(3)	1
O (>FeO)	17.70	17.50(4)	0.071	1
O (>Fe_2O)	16.58	16.72(3)	0.071	1
Fe	15.80	15.95(3)	0.064	0.75(3)
O (>Fe_3O)	15.45	15.60(3)	0.071	1
O	14.02	14.03(2)	0.071	1
Fe	13.67	13.68(2)	0.064	1
O	12.89	12.90(1)	0.071	1
Fe	12.12	12.12(1)	0.064	1
O	11.77	11.77(1)	0.071	1
O	10.335	10.327(5)	0.071	1
Fe	9.985	9.977(5)	0.064	1
O	9.209	9.206(5)	0.071	1
Fe	8.434	8.435(6)	0.064	1
O	8.084	8.085(6)	0.071	1

Layered water structure			
z (Å)	σ_o (Å)	$\overline{\sigma}$ (Å)	d_w (Å)
22.0(1)	0.6(1)	0.4(1)	2.0(2)

Non-structural parameters and quality of fit		
Water film (μm)	Roughness (Å)	χ^2
10[g]	2.4(1)	1.32

For a detailed description of the fitting parameters see Catalano et al. (2006a).

[a] Atom height for the unrelaxed (bulk) structure.

[b] Atom height from the best fit model.

[c] Vibrational amplitude.

[d] Occupancy.

[e] Near-surface oxygen sites are labeled assuming a half-layer termination.

[f] Uncertainties in the last digit are listed in parentheses, reported at the 95% confidence level. Parameters with no listed uncertainties were not varied in the analysis.

[g] Includes the contribution from the 8 μm Kapton film.

and full-layer (~25%) terminations. Accurately measuring the proportion of these two terminations requires refining a structural model that contains both terminations, with each relaxing separately. However, this is not possible because of the limited data range and the correlations that would exist between the parameters in each model from the similar z coordinates of certain atoms [e.g., a site of adsorbed water on the full-layer termination is expected to occur at roughly the same z as the doubly coordinated oxygen site (>Fe_2O) in the half-layer termination]. Thus, the accuracies of the atomic relaxations determined from the X-ray reflectivity data are expected to be worse than the reported precisions. What is clear from the current analysis is that this sample contains a mixture of terminations, with the half-layer termination being dominant. We should note that although the occupancies of the O atoms bound only to the half-layer Fe atom (>FeO and >Fe_2O on the half-layer termination; Fig. 1) also must be less than 1 (they should reduce in proportion to the Fe occupancy), these were not varied to prevent an excessive number of adjustable parameters and because the decrease in the electron density that would results from their removal is likely offset by an increase in electron density from water adsorption on the other termination. As the reflectivity data measures the laterally averaged electron density profile, reducing the occupancies of these O sites in the model without explicit introduction of additional adsorbed water for the full-layer termination would effectively create a ~3 Å vacuum layer over 25% of the surface in the model, which is physically unrealistic.

The termination of the hematite (0 1 2) surface has been recently studied by Tanwar et al. (2007). In that study, the sample was prepared differently (it was not annealed) and measured in humidified He as opposed to under bulk water. Tanwar et al. (2007) observed that the half layer termination was the dominant termination of the surface. We recently observed that a different crystal annealed in air at 450 °C for 24 h expressed the full-layer termination (unpublished data). It thus appears that sample preparation can affect the termination of the hematite (0 1 2) surface found under aqueous conditions and that the occurrence of a mixture of terminations is not intrinsic to the hematite (0 1 2) surface. This will be explored in detail in a future study.

As only the specular X-ray reflectivity data were measured, no lateral relaxations of near-surface atoms could be determined. However, if the singly coordinated oxygen groups on the half-layer termination remain in their bulk positions along b_s, the uppermost FeO_6 octahedra would be distorted (Fig. 3). A relaxation along b_s to above the Fe site would reduce this distortion, and likely be the stable structure in aqueous solution. Such a relaxation is consistent with the XSW imaging results, and will thus be assumed during the remaining analyses.

3.2. Arsenate adsorption geometry

Direct inversion of the measured XSW Fourier components (Fig. 4), each characterized by f_H and P_H values (Table 2), into the coherent interfacial distribution of As was performed using the XSW imaging method. Surface

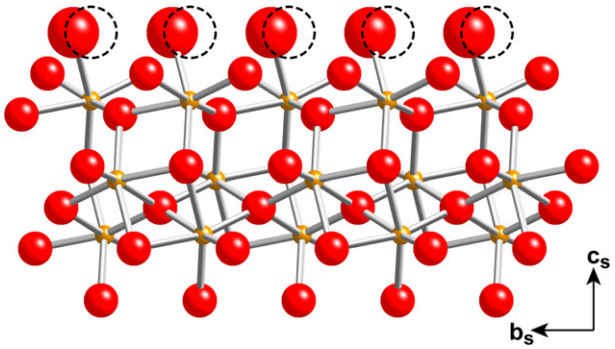

Fig. 3. Structural model of the unrelaxed half-layer termination of the hematite (0 1 2) surface viewed along a_s with the expected locations of the singly coordinated oxygen groups upon relaxation overlain (dashed circles).

symmetry equivalents of the measured reflections were included in the inversion by assuming the appropriate values of f_H and P_H (no symmetry equivalents were measured). The resulting images reveal that As adsorbs primarily above and between the terminal, singly coordinated oxygen groups on pairs of corner-sharing FeO_6 octahedra, ~3 Å above the uppermost plane of Fe atoms of the half-layer termination (Fig. 5). A second, smaller population can be seen in a similar geometry ~2.6 Å above the uppermost plane of Fe atoms of the full-layer termination, reflecting the mixed terminations of this surface. These locations suggest that As adsorbs in a bridging bidentate geometry on adjacent singly coordinated oxygen sites on this surface. The XSW imaging results also reveal that adsorbed As is offset from a symmetrical bridging geometry (i.e., halfway between the singly coordinated oxygen groups with the $O_{surface}$–As–$O_{surface}$ plane normal to the surface), with the two symmetry-related As sites shifted along a_s in opposite direction. Such an offset would result if the arsenate tetrahedra were slightly rotated about an axis created by the pairs of adjacent singly coordinated oxygen groups.

Although the XSW imaging approach provides a model-independent visualization of the location of adsorbed As, the spatial resolution (π/Q_{max}) is only 1.8 Å normal to the surface and 1.3 Å in the surface plane, as it is limited by the number of Fourier components that were measured. More precise, but model-dependent, information regarding the location of As with respect to the surface unit cell was obtained through a least-squares refinement of a structural model compared to the measured P_H and f_H values. The two As sites on each termination observed by XSW imaging were used as initial inputs for the refinement, with their motions related by symmetry ($\Delta x_1 = -\Delta x_2$, $\Delta y_1 = \Delta y_2$, $\Delta z_1 = \Delta z_2$ for each pair). The resulting structural model (Fig. 6, Table 3) differed little from the direct inversion results and reproduced the f_H and P_H values well (Table 4). Inclusion of the As associated with the minor, full-layer termination improved the quality of fit ($\chi^2 = 3.85$) compared to a model with As only on the half-layer termination ($\chi^2 = 9.45$). The total ordered fraction, C, was determined to be 0.58 ± 0.13, with $75 \pm 8\%$ of the arsenic bound to the half-layer termination. This distribution of As between

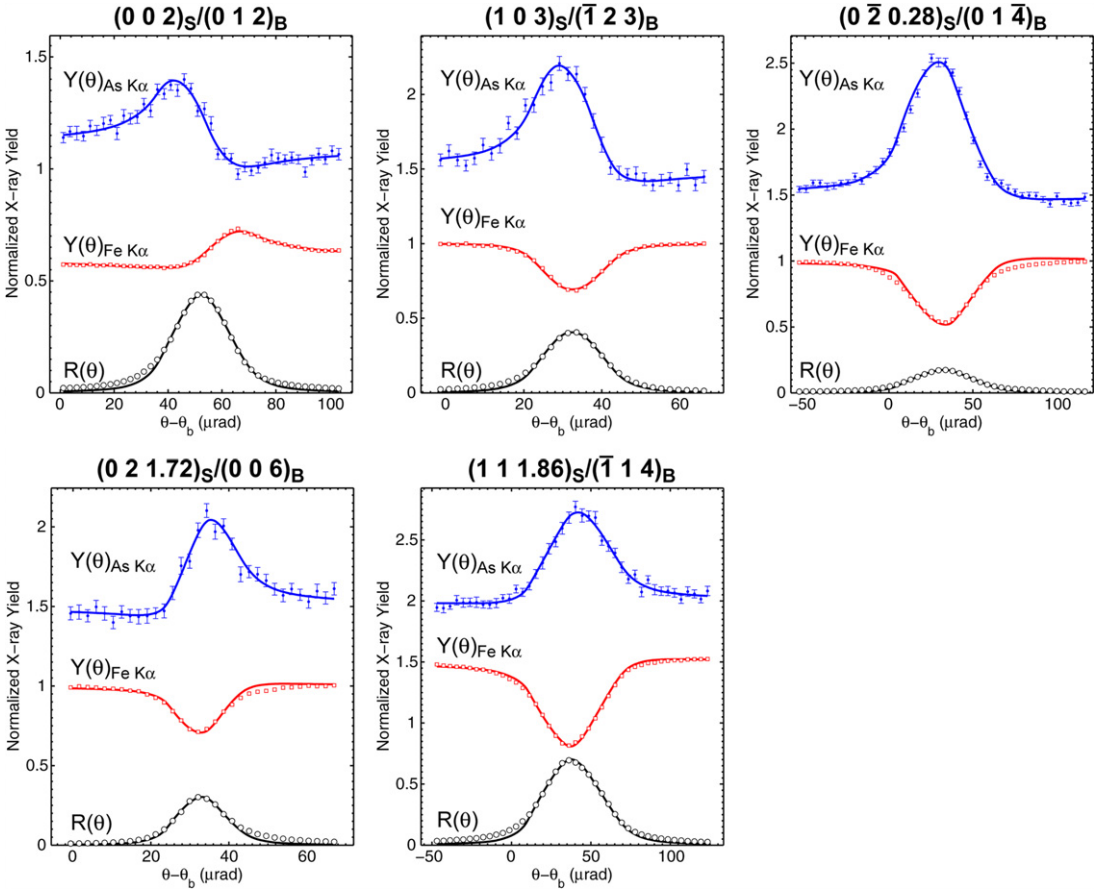

Fig. 4. Experimental $R(\theta)$ and $Y(\theta)$ data and fits to the XSW measurements of arsenate sorbed from a 100 μM solution onto the hematite (0 1 2) surface.

Table 2
XSW measurements of arsenate adsorbed on the hematite (012) surface

Reflection, H (hkl)		d_H (Å)	Q_H (Å^{-1})	As		Fe		
Bulk[a]	Surface[b]			f_H[c]	P_H[c]	f_H[c]	f_{cal}[d]	P_H[c]
(0 1 2)	(0 0 2)	3.69	1.71	0.41(2)	0.15(1)	0.21(1)	0.245	0.50(1)
(0 0 6)	(0 2 1.72)	2.70	2.33	0.28(4)	0.06(3)	0.48(1)	0.65	0[e]
(0 1 4̄)	(0 2̄ 0.28)	2.52	2.49	0.19(2)	0.99(2)	0.59(1)	0.88	0.5[e]
(1̄ 2 3)	(1 0 3)	3.69	1.71	0.54(6)	0.89(2)	0.00(1)	0	0[e]
(1̄ 1 4)	(1 1 1.86)	2.70	2.33	0.14(2)	0.49(4)	0.75(1)	0.88	0.5[e]

[a] Indexing of the bulk structure from Finger and Hazen (1980).
[b] Reindexed with the surface c-axis (c_s) normal to the surface.
[c] The measured coherent fractions and positions with the uncertainties in the last digit, reported at the 95% confidence level, in parentheses.
[d] The calculated coherent fractions for Fe atoms based on the bulk hematite crystal structure assuming $C = 1$ and $D = 1$.
[e] Fixed to their crystallographic values.

the two terminations matches well the proportion of the these terminations determined by X-ray reflectivity. Combining the ordered fraction with the measured As surface coverage of 0.94 ± 0.03 μmol m^{-2} yields a coherent surface coverage of 0.54 ± 0.12 μmol m^{-2}.

The positions of adsorbed As, especially the location of As bound to the minor, full-layer termination, have moderate to large uncertainties, a result of the relatively large number of fitting parameters needed to describe the As distribution as well as correlations between some parameters. Further discussion regarding adsorption geometry is focused on arsenate adsorbed to the dominant, half-layer termination, as this is well constrained. The structural model refinement confirmed that As on the half-layer termination is offset from a symmetrical bridging geometry, with the two As sites displaced ~0.2 Å along a_s in opposite directions from the expected site on the half-layer termination. This offset likely occurs to minimize steric interactions between the unbonded oxygen atoms on the arsenate tetrahedra and nearby doubly coordinated oxygen functional

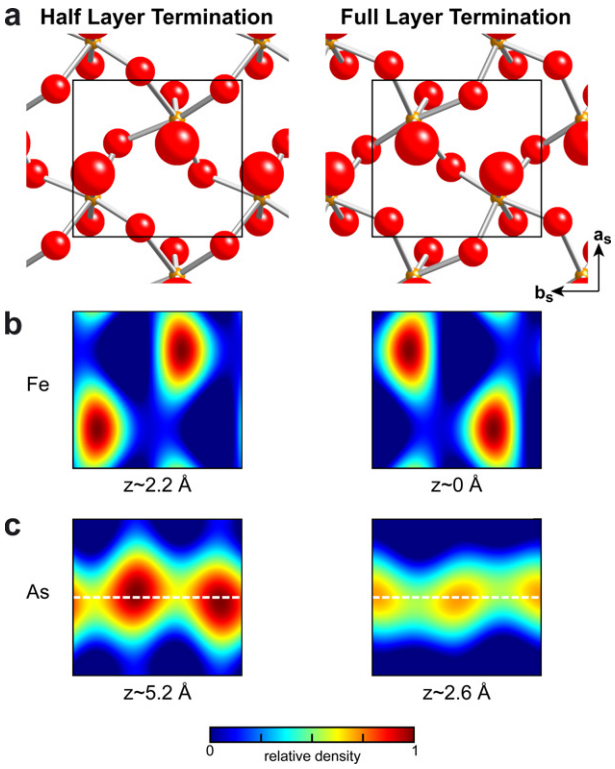

Fig. 5. Results of direct inversion of the XSW data: (a) Top view of the surface unit cells of each termination of the hematite (0 1 2) surface. The small spheres are Fe, the medium spheres O, and large spheres singly coordinated O sites on the surface. (b) Measured lateral distribution of Fe shown as a cut through the maximum density plane for each termination. (c) Measured lateral distribution of As shown as a cut through the maximum density plane above each termination. The white dashed line at $0.5a_s$ is included to highlight the offset of the two maxima in the As density; if As were in a symmetric adsorption geometry these maxima would be on this line.

groups on the hematite surface. This demonstrates that adsorption geometry is affected not just by the functional groups the adsorbate binds to, but also adjacent groups on the surface.

As the X-ray reflectivity data did not provide information on lateral relaxations, and as the presence of two terminations made quantitative analysis of the vertical relaxations difficult and of poor accuracy, atoms on the hematite (0 1 2) surface were assumed to be in their bulk positions when evaluating XSW-derived interatomic distances, with the exception of the positions of the singly coordinated oxygen atoms on the half-layer termination as discussed above. This XSW triangulation-derived structural model results in $As–O_{surface}$ bond lengths of 1.8 ± 0.6 Å, within experimental error of the range of distances (1.66–1.69 Å) commonly seen by EXAFS spectroscopy for As(V) adsorbed on metal oxide surfaces (e.g., Waychunas et al., 1993, 2005a; Fendorf et al., 1997; Arai et al., 2001, 2002, 2004). XSW-derived As–Fe interatomic distances are 3.5 ± 0.4 Å assuming the unrelaxed bulk Fe positions.

3.3. Location of incoherent As

Approximately 40% of the As Kα X-ray fluorescence, corresponding to a surface coverage of 0.40 ± 0.12 μmol m^{-2}, originated from arsenic species not coherently ordered on the hematite (0 1 2) surface. Assuming a 2 μm thick water film above the surface (this was not measured), the equivalent of 0.20 μmol m^{-2} of As exists in the reaction solution. The remaining 0.20 μmol m^{-2} of As may occur sorbed as an outer-sphere species, on disordered defect sites, or in the diffuse layer. The contribution of outer-sphere species to the coherent modulation of the fluorescence yield may be small or negligible at the diffraction conditions used because of the Debye–Waller factor. If we assume that a 10% XSW modulation is detectable, then

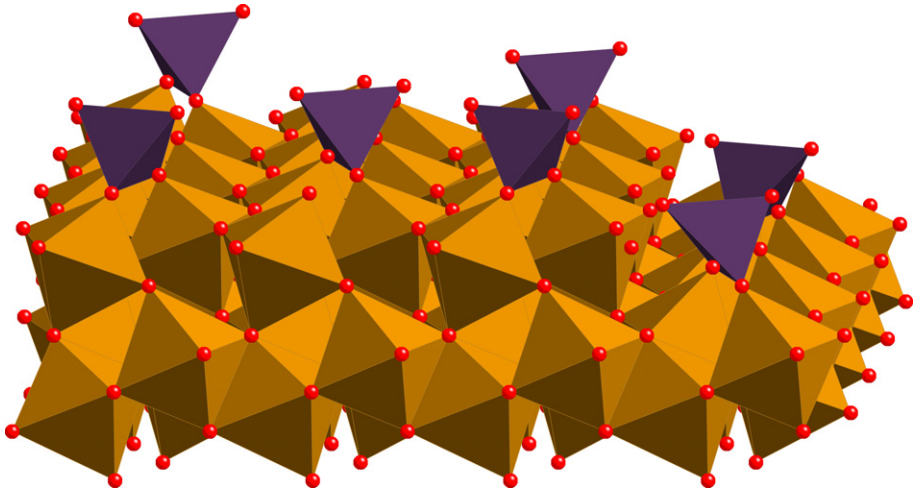

Fig. 6. Schematic model of arsenate surface complexes on hematite (0 1 2) looking down b_s. The step shown on the right side of the figure is included to illustrate the presence of two distinct terminations on the surface. The spatial relationship of these two terminations is unknown.

Table 3
Positions of As (from XSW triangulation fitting), Fe, and O (from bulk crystal structure) in the hematite (0 1 2) surface unit cell

Atom	Half-layer termination			Full-layer termination		
	X (Å)	Y (Å)	Z (Å)[a]	X (Å)	Y (Å)	Z (Å)[a]
Adsorbed arsenate						
As[b]	4.0 ± 0.6	3.5 ± 0.7	5.1 ± 0.2	3 ± 2	2 ± 1	2.6 ± 0.6
As[b]	3.6 ± 0.6	0.8 ± 0.7	5.1 ± 0.2	4 ± 2	4 ± 1	2.6 ± 0.6
Structural atoms[c]						
O	4.27	2.06[d]	4.03	4.27	3.99	1.78
O	3.29	4.77[d]	4.03	3.29	1.28	1.78
O	1.54	3.28	2.91	1.75	4.90	0.35
O	0.91	0.63	2.91	0.77	2.19	0.35
Fe	0.00	2.06	2.13	0.00	4.12	0.00
Fe	2.52	4.77	2.13	2.52	1.41	0.00

[a] Z arbitrarily set to 0 Å for the full-layer iron sites.
[b] Two positions are related by symmetry. Errors shown are at 95% confidence level.
[c] O and Fe positions are unrelaxed bulk atom locations for hematite, except where specified.
[d] O positions relaxed along b_s as shown in Fig. 3.

Table 4
Comparison of measured and refined XSW results for As in a bridging bidentate geometry

Reflection, H (hkl)		XSW data		Triangulation results		χ^2
Bulk	Surface	f_H	P_H	f_{opt}	P_{opt}	
(0 1 2)	(0 0 2)	0.41	0.15	0.39	0.15	3.85
(0 0 6)	(0 2 1.72)	0.28	0.06	0.44	0.05	
(0 1 $\bar{4}$)	(0 $\bar{2}$ 0.28)	0.19	0.99	0.29	0.96	
($\bar{1}$ 2 3)	(1 0 3)	0.54	0.89	0.51	0.89	
($\bar{1}$ 1 4)	(1 1 1.86)	0.14	0.49	0.03	0.50	

for the Bragg reflections with the smallest Q value (1.71 Å^{-1}), a single outer-sphere species at this coverage would need to have a vibrational amplitude less than 0.7 Å to be observable. If the detection limit is raised to a 20% XSW modulation, then this maximum vibrational amplitude drops to 0.2 Å. The vibrational amplitude constraints become even smaller when considering the Bragg reflections with larger Q values. Thus, an outer-sphere species occurring at the fractional coverage of the incoherent As would need to have low positional disorder with respect to the crystal lattice to be observed by XSW, which is unlikely as such species lack a direct bond to the surface.

The contribution to the XSW modulation from arsenic adsorbed onto defect sites will depend on the nature of the defect. Defects such as steps, kinks, and vacancies are likely ordered with respect to the underlying crystal structure, and arsenate binding to such sites in appreciable quantities would therefore be detectable by XSW measurements. On this sample, the density of binding sites on steps can be estimated from the surface domain size ($> \sim 6500$ Å). For a surface unit cell surface length of $\sim$5 Å, this domain size suggests that a step is present every 1300 unit cells. If we assume a step has the same density of binding sites as a unit cell [7.3 sites nm^{-2}, based on singly coordinated oxygen sites per hematite (0 1 2) surface unit cell], then this corresponds to a binding site density on steps of 0.009 μmol m^{-2}, more than an order of magnitude less than the coverage of the incoherent adsorbed As. Adsorption onto defects not ordered with respect to the hematite lattice, such as those at grain boundaries, would contribute to the incoherent adsorbed As signal. Similarly, As in a diffuse layer would appear disordered in the XSW derived from a Bragg reflection from the hematite lattice. Although the location of this unconstrained fraction of adsorbed As cannot be determined from the present data, it appears to be in a more disordered form (either weakly bound or on disordered sites) than the inner-sphere bridging bidentate complexes observed with the XSW measurements.

3.4. Comparisons to past studies

Past experimental studies of As(V) adsorption onto iron, aluminum, manganese, and titanium (oxyhydr)oxides have consistently observed the formation of inner-sphere adsorption complexes (Waychunas et al., 1993, 1995, 1996, 2005a; Manceau, 1995; Sun and Doner, 1996; Fendorf et al., 1997; Arai et al., 2001, 2002, 2004; Goldberg and Johnston, 2001; Ladeira et al., 2001; O'Reilly et al., 2001; Randall et al., 2001; Farquhar et al., 2002; Manning et al., 2002a; Foster et al., 2003; Sherman and Randall, 2003; Pena et al., 2006). In all experimental studies that were sensitive to the local atomic environment of the adsorbate, bridging bidentate (i.e., bidentate binuclear) complexes were observed. A subset of these studies (Manceau, 1995; Fendorf et al., 1997; Randall et al., 2001; Waychunas et al., 2005a) have also observed the formation of edge-sharing bidentate (i.e., bidentate mononuclear) complexes on goethite, although there is still some debate about whether

these actually form (Sherman and Randall, 2003). Monodentate arsenate complexes have also been observed to form, primarily at low surface coverages (Waychunas et al., 1993; Fendorf et al., 1997). In most past EXAFS spectroscopy studies where multiple surface complexes were identified (e.g., Waychunas et al., 1993; Manceau, 1995; Fendorf et al., 1997), the number of Fe neighbors identified was often significantly larger than that expected for purely adsorbed arsenate. This suggests that in such studies an Fe–As precipitate formed, the FEFF-derived EXAFS fitting functions were not correct, erroneous Debye–Waller factors were used, or features in the EXAFS spectra were misidentified [e.g., Sherman and Randall (2003) suggested that the feature previously identified as due to an Fe neighbor at ~2.85 Å is actually produced by multiple scattering]. Inner-sphere arsenate surface complexes have also been identified in contaminated soils and soils overlying geochemical anomalies, mine tailings, cement-stabilized sludge, water treatment adsorbents, and iron corrosion products (Foster et al., 1998; Savage et al., 2000; Farrell et al., 2001; Manning et al., 2002b; Morin et al., 2002; Jing et al., 2003, 2005; Moldovan et al., 2003; Paktunc et al., 2003, 2004; Beaulieu and Savage, 2005; Cances et al., 2005).

In many of these past studies, the adsorption geometry has been inferred based on arsenic–metal cation interatomic distances obtained from EXAFS spectroscopy. For iron (oxyhydr)oxides, As–Fe distances of ~2.85, ~3.25, and ~3.60 Å have identified the presence of edge-sharing bidentate, bridging bidentate, and monodentate complexes, respectively. These distances are derived from studies of arsenate adsorption onto goethite. However, the As–Fe distances observed in this study (3.5 ± 0.4 Å) are intermediate between the distances expected for bridging bidentate and monodentate complexes. These distances are longer than, although within error of, those typically expected for bridging bidentate complexes because the FeO_6 octahedra are arranged differently on hematite surfaces than on goethite surface. In fact, the model of bidentate arsenate corner-sharing between two adjacent edge-sharing FeO_6 octahedra often used in molecular modeling and interpreting EXAFS data, as in Sherman and Randall (2003), cannot exist on any known rational termination of hematite. Adjacent edge-sharing FeO_6 octahedra are never exposed in a way that both would have singly coordinated oxygens available to bind to the same As atom, except perhaps on a step or other surface defect. The adjacent FeO_6 octahedra arsenate binds to on the hematite (0 1 2) surface, and likely on most other hematite surfaces, are corner-sharing. This demonstrates that the As–Fe distances resulting from the formation of bridging bidentate surface complexes are dependent on the sorbent structure, and that geometries different from those considered in past studies are possible. For systems where arsenate is sorbing to Fe(III)-bearing phases lacking goethite-like polyhedral arrangements or to nanoscale phases where polyhedra may be distorted (e.g., Waychunas et al., 2005b), multiple arrangements of FeO_6 and AsO_4 polyhedra should be considered when assigning adsorbate binding modes from EXAFS data.

One other study to date has examined arsenate adsorption onto the hematite (0 1 2) surface using ex situ GI-EXAFS measurements (Waychunas et al., 2005a), inferring that $78 \pm 10\%$ of the adsorbed arsenate was in edge-sharing bidentate complexes, with the remainder in bridging bidentate complexes. It is unclear if the discrepancy between that study and the current work is the result of different measurement conditions [this study was performed under aqueous solution, the Waychunas et al. (2005a) study in humidified He], or if the GI-EXAFS data were misinterpreted, as the As–Fe distance characteristic of edge-sharing complexes was identified for only one polarization direction and was atypically short (2.75 ± 0.02 Å). In addition, the analysis of surface domain size and step density discussed above demonstrates that the number of available binding sites on steps (where edge-sharing complexation may be more favorable) is too small to account for the edge-sharing complexes identified on a similarly prepared sample by Waychunas et al. (2005a). If such complexes formed on ordered sites on the hematite (0 1 2) surface, they would have vibrational amplitudes comparable to that of the bridging bidentate complexes, and thus would have been observed by the XSW measurements. It is difficult to further evaluate potential sources of error in the GI-EXAFS analyses in Waychunas et al. (2005a), as they do not report the raw GI-EXAFS spectra of As(V) sorbed to the hematite (0 1 2) surface. However, as demonstrated above, the three-dimensional relationship of an adsorbate to the structure of the substrate is directly imaged from XSW measurements, whereas GI-EXAFS measurements require this relationship to be inferred from fitting results that can be highly model-dependent. Our analyses show that the edge-sharing complex of As proposed by Waychunas et al. (2005a) is not the dominant species of As adsorbed to hematite (0 1 2) in contact with an aqueous solution, suggesting that these edge-sharing complexes were either an artifact of the ex situ measurement conditions or were identified incorrectly.

3.5. Preferred binding site, adsorption geometry, and reaction stoichiometry

The XSW measurements presented here are the first to directly determine the relationship of adsorbed arsenate to the structure of an iron (oxyhydr)oxide sorbent. These results demonstrate that the dominant form of adsorbed arsenate binds exclusively to singly coordinated oxygen functional groups on both terminations of the hematite (0 1 2) surface. As multiple types of functional groups are present on the hematite (0 1 2) surface, this suggests that arsenate preferentially reacts with the singly coordinated oxygen groups. The reason for this preference may be steric (i.e., doubly and triply coordinated groups may not be accessible), energetic, or kinetic (e.g., faster exchange kinetics of singly coordinated functional groups). These results also demonstrate that arsenate dominantly forms bridging bidentate surface complexes on hematite (0 1 2). Considering the ubiquitous identification of bridging bidentate arsenate surface complexes on iron, aluminum, manganese, and titanium (oxyhydr)oxide phases (see discussion in Section 3.4), it is likely that this is the preferred adsorption geometry of arsenate.

Identification of the inner-sphere binding site and adsorption geometry of arsenate on the hematite (0 1 2) sur-

face provides enough information to constrain the possible stoichiometry of the reaction occurring at pH 5 to the following:

$$2{>}\mathrm{FeOH} + \mathrm{H_2AsO_4} + n\mathrm{H^+} = (>\mathrm{FeO})_2\mathrm{AsO_2H}_n^{n-1} + 2\mathrm{H_2O} \quad (2)$$

Although the choice of arsenate dissociation state is arbitrary when writing such a reaction, as it is related to all other possible states through equilibrium reactions, the state used in reaction (2) was chosen to reflect the likely predominant species present under the conditions of this study [arsenate has pK_a values of 2.2, 6.9, and 11.5 (Baes and Mesmer, 1986)]. The choice of surface protonation state is also arbitrary (i.e., all protonation states are related through equilibrium reactions); here we use a neutral surface site from a simple 2-pK_a model of surface functional group protonation/deprotonation (Schindler and Stumm, 1987). The real protonation state (and charge) of singly coordinated functional groups on the hematite (0 1 2) surface is not accessible through our measurements, and prediction of this state will depend on the parameters obtained from modeling the charging behavior of this surface, which has yet to be measured. The experimentally-determined pH_{iep} of the α-Al_2O_3 (0 1 2) surface (which has a similar distribution of surface functional groups) is 4.5–5.2 (Franks and Meagher, 2003; Kershner et al., 2004; Fitts et al., 2005) and the measured pH_{iep} of a single crystal of hematite (multiple crystal faces) is 6.1 (Kallay et al., 2005), suggesting that in this study the hematite (0 1 2) surface was near its isoelectric point. The protonation state of the arsenate surface complex also cannot be determined from the XSW measurements, and thus the proton stoichiometry cannot be established. However, a recent surface complexation modeling study by Fukushi and Sverjensky (2007) predicted that on hematite powders the dominant arsenate surface species under similar conditions will be a fully deprotonated bridging bidentate complex. We expect arsenate species on the hematite (0 1 2) surface to behave similarly.

The sample used in this study also provided the opportunity to compare the reactivity of singly coordinated oxygen functional groups on the two terminations present. The excellent agreement between the proportion of the two terminations ($75 \pm 3\%$ half-layer termination) and the distribution of the inner-sphere arsenate on the two terminations ($75 \pm 8\%$ on the half-layer terminations) suggest that these functional groups have an equal reactivity towards the adsorption of arsenate. This was not necessarily expected, as the two terminations have a different distribution of oxygen functional groups on the surface, and thus a different distribution of charges and hydrogen bonds. Although doubly (on the half-layer termination) and triply (on the full-layer termination) coordinated oxygen functional groups appear to have minor steric interactions with adsorbed arsenate, causing the offset from a symmetric adsorption geometry as described above, these interactions either make a minimal contribution in determining the stability of the arsenate surface complexes, or the effects on stability are equivalent on the two terminations even though different functional groups are involved.

3.6. Implications for As mobility in the environment

Under conditions similar to those used in this study, arsenate fate, transport, and bioavailability will likely be controlled primarily by the formation of bridging bidentate surface complexes in systems where iron (oxyhydr)oxides are present. The apparent dominance of such complexes on aluminum, iron, manganese, and titanium (oxyhydr)oxide surfaces suggests that modeling the adsorption behavior of arsenate in complex environmental systems should be straightforward. However, as we observed that a significant fraction of adsorbed arsenate is not coherently adsorbed, and thus cannot be characterized by XSW, further experimental work is needed to identify what other adsorbed species are present. As such species occur in a more disordered form, it is possible they are more weakly bound, and may thus dominate that fraction of arsenate that may be remobilized and made bioavailable.

3.7. Prospects for species-specific XSW

The off-Bragg yield, Y_{OB}, is a measure of the X-ray fluorescence induced by the incident X-ray beam away from dynamical diffraction conditions. The variation in Y_{OB} with incident X-ray energy is thus proportional to the XANES spectrum of the element of interest. XSW measurements for the $(0\,0\,2)_s$ reflection near the As K-edge demonstrate this modulation in Y_{OB} (Fig. 7). In particular, the data show clear consistency between the observed variation in Y_{OB} with the energy-dependent X-ray absorption of As. By tuning the incident X-ray beam energy to a feature in a XANES spectrum indicative of a specific oxidation state of an element (e.g., As(III) whiteline, Cr(VI) pre-edge feature), it will be possible to measure an oxidation

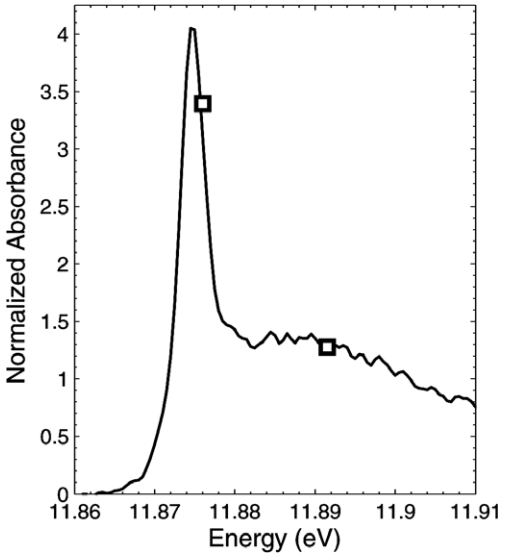

Fig. 7. Fluorescence-yield XANES spectrum of arsenate adsorbed on the hematite (0 1 2) surface. The two open squares are Y_{OB} values determined from XSW measurements made at those energies. These values were converted to normalized absorbance by setting the high-energy Y_{OB} value equal to the normalized absorbance at that energy.

state-specific XSW profile. Thus, XSW measurements can provide insight into the mechanisms of surface-catalyzed redox changes by determining how both reduced and oxidized forms of an element associate with the surface, even when multiple valence states are present simultaneously.

4. CONCLUSIONS

This study sought to determine the three-dimensional relationship of adsorbed arsenate to the structure of, and thus the functional groups on, the hematite (0 1 2) surface in aqueous solution. Characterization of the hematite surface reveals a mixture of a dominant half-layer and minority full-layer termination (75% and 25% of the surface, respectively). The coexistence of two terminations appears to be due to sample preparation, and is not a unique attribute of the hematite (0 1 2) surface. Structural relaxations are minor (<0.15 Å), and water ordering at the hematite (0 1 2)-aqueous solution interface is similar to what was recently observed for the corundum (0 1 2) surface (Catalano et al., 2006a).

XSW measurements demonstrate that arsenate adsorbs on the (0 1 2) surface of hematite by forming inner-sphere bridging bidentate complexes bound to singly coordinated oxygen functional groups. Arsenate was found to distribute itself between the two surface terminations in proportion to their occurrence, suggesting both terminations have an equal affinity for the adsorption of this species. No evidence was found for the formation of edge-sharing bidentate or monodentate complexes. Such complexes may form on surface defects not ordered with respect to the hematite lattice, which do not contribute to the XSW modulations; they are not present on terraces on this surface under the conditions studied. Approximately 25% of the arsenate associated with the surface (i.e., the arsenate not in the solution phase) was not coherently sorbed, and thus was most likely bound to disordered surface defects, as outer-sphere species, or in the diffuse layer.

Although, the adsorption geometry observed in this study is consistent with the dominant geometry observed in past studies, the resulting As–Fe distances are longer than typically seen for bridging bidentate surface complexes on iron (oxyhydr)oxides. This demonstrates that proper interpretation of the EXAFS spectra of adsorbates, the most common method for determining adsorbate structure, requires a detailed understanding of the surface structure of the sorbent phase. Without this consideration, it is possible to misidentify the binding geometry of arsenate in environmental samples, which would result in the assumption of incorrect reaction stoichiometries and possibly lead to erroneous prediction of future fate and transport.

This study is the first to directly measure the full-structural relationship of adsorbed arsenate to the crystal structure of an iron (oxyhydr)oxide sorbent phase, with knowledge of both the mineral surface structure and the location of the adsorbed species. These results suggest that arsenate prefers to bind to singly coordinated oxygen groups in a bridging bidentate geometry, and constrain the likely adsorption reaction stoichiometry. Although bridging bidentate surface complexes are the dominant form observed in this and past studies, yet to be identified minor sorbed arsenate species also are present, and are potentially the most important species affecting arsenate fate, transport, and bioavailability. Finally, we have demonstrated that the off-Bragg fluorescence yield, Y_{OB}, obtained from XSW measurements tracks the XANES spectrum of the fluorescing element, and that by tuning to the correct incident energy, species-specific XSW measurements can be made.

ACKNOWLEDGMENTS

Peter Eng and Sanjit Ghose (GSECARS) are thanked for providing the hematite sample. Comments from George Calas and an anonymous reviewer improved this manuscript. This work was supported by the ANL Named Postdoctoral Fellowship Program and the Geosciences Research Program of the Office of Basic Energy Sciences, U.S. Department of Energy (DOE), through Contract DE-AC-02-06CH11357 to ANL. The data were measured at beamlines 12-ID-D and 12-BM of the Basic Energy Sciences Synchrotron Radiation Center (BESSRC/XOR), APS. Use of the APS was supported by the U.S. DOE, Office of Science, Office of Basic Energy Sciences, under Contract No. DE-AC02-06CH11357.

REFERENCES

Arai Y., Elzinga E. J., and Sparks D. L. (2001) X-ray absorption spectroscopic investigation of arsenite and arsenate adsorption at the aluminum oxide-water interface. *J. Colloid Interface Sci.* **235**, 80–88.

Arai Y., and Sparks D. L. (2002) Residence time effects on arsenate surface speciation at the aluminum oxide-water interface. *Soil Sci.* **167**, 303–314.

Arai Y., Sparks D. L., and Davis J. A. (2004) Effects of dissolved carbonate on arsenate adsorption and surface speciation at the hematite-water interface. *Environ. Sci. Technol.* **38**, 817–824.

Azcue J. M., and Nriagu J. O. (1993) Arsenic forms in mine-polluted sediments of Moira Lake, Ontario. *Environ. Int.* **19**, 405–415.

Baes C. F., and Mesmer R. E. (1986) *The Hydrolysis of Cations*. Robert F. Krieger Publishing Co., Malabar, FL.

Batterman B. W. (1964) Effect of dynamical diffraction in X-ray fluorescence scattering. *Phys. Rev. A* **133**, A759–A764.

Beaulieu B. T., and Savage K. S. (2005) Arsenate adsorption structures on aluminum oxide and phyllosilicate mineral surfaces in smelter-impacted soils. *Environ. Sci. Technol.* **39**, 3571–3579.

Bedzyk M. J., and Materlik G. (1985a) X-ray standing wave analysis for bromine chemisorbed on germanium. *Surf. Sci.* **152**, 10–16.

Bedzyk M. J., and Materlik G. (1985b) Determination of the position and vibrational amplitude of an adsorbate by means of multiple-order X-ray standing wave measurements. *Phys. Rev. B* **31**, 4110–4112.

Bedzyk M. J., and Cheng L. (2002) X-ray standing wave studies of minerals and mineral surfaces: Principles and applications. *Rev. Mineral. Geochem.* **49**, 221–266.

Bedzyk M. J., Bommarito G. M., Caffrey M., and Penner T. L. (1990) Diffuse-double layer at a membrane-aqueous interface measured with X-ray standing waves. *Science* **248**, 52–56.

Beno M. A., Engbretson M., Jennings G., Knapp G. S., Linton J., Kurtz C., Rutt U., and Montano P. A. (2001a) BESSRC-CAT bending magnet beamline at the Advanced Photon Source. *Nucl. Instrum. Methods Phys. Res., Sec. A* **467**, 699–702.

Beno M. A., Jennings G., Engbretson M., Knapp G. S., Kurtz B., Zabransky B., Linton J., Seifert S., Wiley C., and Montano P. A. (2001b) Basic energy sciences synchrotron radiation center undulator sector at the advanced photon source. *Nucl. Instrum. Methods Phys. Res., Sec. A* **467**, 690–693.

Cances B., Juillot F., Morin G., Laperche V., Alvarez L., Proux O., Hazemann J. L., Brown, Jr., G. E., and Calas G. (2005) XAS evidence of As(V) association with iron oxyhydroxides in a contaminated soil at a former arsenical pesticide processing plant. *Environ. Sci. Technol.* **39**, 9398–9405.

Carlson L., Bigham J. M., Schwertmann U., Kyek A., and Wagner F. (2002) Scavenging of As from acid mine drainage by schwertmannite and ferrihydrite: a comparison with synthetic analogues. *Environ. Sci. Technol.* **36**, 1712–1719.

Catalano J. G., Park C., Zhang Z., and Fenter P. (2006a) Termination and water adsorption at the α-Al_2O_3 (012)-aqueous solution interface. *Langmuir* **22**, 4668–4673.

Catalano J. G., Zhang Z., Fenter P., and Bedzyk M. J. (2006b) Inner-sphere surface complexation of Se(IV) on the hematite (100) surface. *J. Colloid Interface Sci.* **297**, 665–671.

Cheng L., Fenter P., Bedzyk M. J., and Sturchio N. C. (2003) Fourier-expansion solution of atom distributions in a crystal using X-ray standing waves. *Phys. Rev. Lett.* **90**, 255503.

Cornell R. M., and Schwertmann U. (2003) *The Iron Oxides: Structure, Properties, Reactions, Occurrences, and Uses*. Wiley-VCH, Weinheim.

Courtin-Nomade A., Bril H., Neel C., and Lenain J. F. (2003) Arsenic in iron cements developed within tailings of a former metalliferous mine - Enguiales, Aveyron, France. *Appl. Geochem.* **18**, 395–408.

Courtin-Nomade A., Grosbois C., Bril H., and Roussel C. (2005) Spatial variability of arsenic in some iron-rich deposits generated by acid mine drainage. *Appl. Geochem.* **20**, 383–396.

Devitre R., Belzile N., and Tessier A. (1991) Speciation and adsorption of arsenic on diagenetic iron oxyhydroxides. *Limnol. Oceanogr.* **36**, 1480–1485.

Donahue R., and Hendry M. J. (2003) Geochemistry of arsenic in uranium mine mill tailings, Saskatchewan, Canada. *Appl. Geochem.* **18**, 1733–1750.

Farquhar M. L., Charnock J. M., Livens F. R., and Vaughan D. J. (2002) Mechanisms of arsenic uptake from aqueous solution by interaction with goethite, lepidocrocite, mackinawite, and pyrite: an X-ray absorption spectroscopy study. *Environ. Sci. Technol.* **36**, 1757–1762.

Farrell J., Wang J. P., O'Day P., and Conklin M. (2001) Electrochemical and spectroscopic study of arsenate removal from water using zero-valent iron media. *Environ. Sci. Technol.* **35**, 2026–2032.

Fendorf S., Eick M. J., Grossl P., and Sparks D. L. (1997) Arsenate and chromate retention mechanisms on goethite. 1. Surface structure. *Environ. Sci. Technol.* **31**, 315–320.

Fenter P. (2002) X-ray reflectivity as a probe of mineral-fluid interfaces: a user guide. *Rev. Mineral. Geochem.* **49**, 149–220.

Fenter P., Catalano J. G., Park C., and Zhang Z. (2006) On the use of CCD area detectors for high resolution specular X-ray reflectivity. *J. Synchrotron Radiat.* **13**, 293–303.

Finger L. W., and Hazen R. M. (1980) Crystal structure and isothermal compression of Fe_2O_3, Cr_2O_3, and V_2O_3 to 50 kbars. *J. Appl. Phys.* **51**, 5362–5367.

Fitts J. P., Shang X. M., Flynn G. W., Heinz T. F., and Eisenthal K. B. (2005) Electrostatic surface charge at aqueous/α-Al_2O_3 single-crystal interfaces as probed by optical second-harmonic generation. *J. Phys. Chem. B* **109**, 7981–7986.

Foster A. L., Brown, Jr., G. E., Tingle T. N., and Parks G. A. (1998) Quantitative arsenic speciation in mine tailings using X-ray absorption spectroscopy. *Am. Mineral.* **83**, 553–568.

Foster A. L., Brown, Jr., G. E., and Parks G. A. (2003) X-ray absorption fine structure study of As(V) and Se(IV) sorption complexes on hydrous Mn oxides. *Geochim. Cosmochim. Acta* **67**, 1937–1953.

Franks G. V., and Meagher L. (2003) The isoelectric points of sapphire crystals and alpha-alumina powder. *Colloids Surf., A* **214**, 99–110.

Fukushi K., Sasaki M., Sato T., Yanase N., Amano H., and Ikeda (2003) A natural attenuation of arsenic in drainage from an abandoned arsenic mine dump. *Appl. Geochem.* **18**, 1267–1278.

Fukushi, K., Sverjensky, D.A. (2007) A predictive model (ETLM) for arsenate adsorption and surface speciation on oxides consistent with spectroscopic and theoretical molecular evidence. *Geochim. Cosmochim. Acta* (submitted for publication).

Garelick H., Dybowska A., Valsami-Jones E., and Priest N. D. (2005) Remediation technologies for arsenic contaminated drinking waters. *J. Soils Sediments* **5**, 182–190.

Geissbuhler P., Fenter P., DiMasi E., Srajer G., Sorensen L. B., and Sturchio N. C. (2004) Three-dimensional structure of the calcite-water interface by surface X-ray scattering. *Surf. Sci.* **573**, 191–203.

Goldberg S. (1986) Chemical modeling of arsenate adsorption on aluminum and iron oxide minerals. *Soil Sci. Soc. Am. J.* **50**, 1154–1157.

Goldberg S., and Johnston C. T. (2001) Mechanisms of arsenic adsorption on amorphous oxides evaluated using macroscopic measurements, vibrational spectroscopy, and surface complexation modeling. *J. Colloid Interface Sci.* **234**, 204–216.

Golovchenko J. A., Patel J. R., Kaplan D. R., Cowan P. L., and Bedzyk M. J. (1982) Solution to the surface registration problem using X-ray standing waves. *Phys. Rev. Lett.* **49**, 560–563.

Grossl P. R., and Sparks D. L. (1995) Evaluation for contaminant ion adsorption/desorption on goethite using pressure-jump relaxation kinetics. *Geoderma* **67**, 87–101.

Grossl P. R., Eick M., Sparks D. L., Goldberg S., and Ainsworth C. C. (1997) Arsenate and chromate retention mechanisms on goethite. 2. Kinetic evaluation using a pressure-jump relaxation technique. *Environ. Sci. Technol.* **31**, 321–326.

Hartman P. (1989) The effect of surface relaxation on crystal habit: Cases of corundum (α-Al_2O_3) and hematite (α-Fe_2O_3). *J. Cryst. Growth* **96**, 667–672.

Hertel N., Materlik G., and Zegenhagen J. (1985) X-ray standing wave analysis of bismuth implanted in Si(110). *Z. Phys. B* **58**, 199–204.

Hiemstra T., and Van Riemsdijk W. H. (1996) A surface structural approach to ion adsorption: the charge distribution (CD) model. *J. Colloid Interface Sci.* **179**, 488–508.

Hiemstra T., and Van Riemsdijk W. H. (1999) Surface structural ion adsorption modeling of competitive binding of oxyanions by metal (hydr)oxides. *J. Colloid Interface Sci.* **210**, 182–193.

Jain A., Raven K. P., and Loeppert R. H. (1999) Arsenite and arsenate adsorption on ferrihydrite: Surface charge reduction and net OH^- release stoichiometry. *Environ. Sci. Technol.* **33**, 1179–1184.

Jessen S., Larsen F., Koch C. B., and Arvin E. (2005) Sorption and desorption of arsenic to ferrihydrite in a sand filter. *Environ. Sci. Technol.* **39**, 8045–8051.

Jing C. Y., Korfiatis G. P., and Meng X. G. (2003) Immobilization mechanisms of arsenate in iron hydroxide sludge stabilized with cement. *Environ. Sci. Technol.* **37**, 5050–5056.

Jing C. Y., Liu S. Q., Patel M., and Meng X. G. (2005) Arsenic leachability in water treatment adsorbents. *Environ. Sci. Technol.* **39**, 5481–5487.

Kallay N., Dojnovic Z., and Cop A. (2005) Surface potential at the hematite-water interface. *J. Colloid Interface Sci.* **286**, 610–614.

Katsoyiannis I. A., and Zouboulis A. I. (2002) Removal of arsenic from contaminated water sources by sorption onto iron-oxide-coated polymeric materials. *Water Res.* **36**, 5141–5155.

Kershner R. J., Bullard J. W., and Cima M. J. (2004) Zeta potential orientation dependence of sapphire substrates. *Langmuir* **20**, 4101–4108.

Ladeira A. C. Q., Ciminelli V. S. T., Duarte H. A., Alves M. C. M., and Ramos A. Y. (2001) Mechanism of anion retention from EXAFS and density functional calculations: Arsenic (V) adsorbed on gibbsite. *Geochim. Cosmochim. Acta* **65**, 1211–1217.

Linge K. L., and Oldham C. E. (2004) Control mechanisms for dissolved phosphorus and arsenic in a shallow lake. *Appl. Geochem.* **19**, 1377–1389.

Mackrodt W. C., Davey R. J., Black S. N., and Docherty R. (1987) The morphology of α-Al_2O_3 and α-Fe_2O_3: the importance of surface relaxation. *J. Cryst. Growth* **80**, 441–446.

Manceau A. (1995) The mechanism of anion adsorption on iron oxides: evidence for the bonding of arsenate tetrahedra on free $Fe(O, OH)_6$ edges. *Geochim. Cosmochim. Acta* **59**, 3647–3653.

Manning B. A., Fendorf S. E., Bostick B., and Suarez D. L. (2002a) Arsenic(III) oxidation and arsenic(V) adsorption reactions on synthetic birnessite. *Environ. Sci. Technol.* **36**, 976–981.

Manning B. A., Hunt M. L., Amrhein C., and Yarmoff J. A. (2002b) Arsenic(III) and Arsenic(V) reactions with zerovalent iron corrosion products. *Environ. Sci. Technol* **36**, 5455–5461.

Moldovan B. J., Jiang D. T., and Hendry M. J. (2003) Arsenic in uranium mine tailings precipitated from iron-rich hydrometallurgical solutions. *Environ. Sci. Technol.* **37**, 873–879.

Morin G., Lecocq D., Juillot F., Calas G., Ildefonse P., Belin S., Briois V., Dillmann P., Chevallier P., Gauthier C., Sole A., Petit P.-E., and Borensztajn S. (2002) EXAFS evidence of sorbed arsenic(V) and pharmacoside rite in a soil overlying the Echassières geochemical anomaly, Allier, France. *Bull. Soc. Géol. France* **173**, 281–291.

Morin G., Juillot F., Casiot C., Bruneel O., Personné J. C., Elbaz-Poulichet F., Leblanc M., Ildefonse P., and Calas G. (2003) Bacterial formation of tooeleite and mixed arsenic(III) or arsenic(V)-iron(III) gels in the Carnoulès acid mine drainage, France. A XANES, XRD, and SEM study. *Environ. Sci. Technol.* **37**, 1705–1712.

Okasinski J. S., Kim C., Walko D. A., and Bedzyk M. J. (2004) X-ray standing wave imaging of the 1/3 monolayer Sn/Ge-(1 1 1) surface. *Phys. Rev. B* **69**, 041401.

O'Reilly S. E., Strawn D. G., and Sparks D. L. (2001) Residence time effects on arsenate adsorption/desorption mechanisms on goethite. *Soil Sci. Soc. Am. J.* **65**, 67–77.

Paktunc D., Foster A., and Laflamme G. (2003) Speciation and characterization of arsenic in Ketza River mine tailings using X-ray absorption spectroscopy. *Environ. Sci. Technol.* **37**, 2067–2074.

Paktunc D., Foster A., Heald S., and Laflamme G. (2004) Speciation and characterization of arsenic in gold ores and cyanidation tailings using X-ray absorption spectroscopy. *Geochim. Cosmochim. Acta* **68**, 969–983.

Pauling L. (1960) *The Nature of the Chemical Bond*. Cornell University Press, Ithaca.

Pena M., Meng X. G., Korfiatis G. P., and Jing C. Y. (2006) Adsorption mechanism of arsenic on nanocrystalline titanium dioxide. *Environ. Sci. Technol.* **40**, 1257–1262.

Pichler T., and Veizer J. (1999) Precipitation of Fe(III) oxyhydroxide deposits from shallow-water hydrothermal fluids in Tutum Bay, Ambitle Island, Papua New Guinea. *Chem. Geol.* **162**, 15–31.

Polizzotto M. L., Harvey C. F., Sutton S. R., and Fendorf S. (2005) Processes conducive to the release and transport of arsenic into aquifers of Bangladesh. *Proc. Natl. Acad. Sci. USA* **102**, 18819–18823.

Randall S. R., Sherman D. M., and Ragnarsdottir K. V. (2001) Sorption of As(V) on green rust ($Fe_4(II)Fe_2(III)(OH)_{12}SO_4 \cdot 3H_2O$) and lepidocrocite ($\gamma$-FeOOH): surface complexes from EXAFS spectroscopy. *Geochim. Cosmochim. Acta* **65**, 1015–1023.

Savage K. S., Tingle T. N., O'Day P. A., Waychunas G. A., and Bird D. K. (2000) Arsenic speciation in pyrite and secondary weathering phases, Mother Lode Gold District, Tuolumne County, California. *Appl. Geochem.* **15**, 1219–1244.

Schindler P. W., and Stumm W. (1987) The surface chemistry of oxides, hydroxides and oxide minerals. In *Aquatic Surface Chemistry* (ed. W. Stumm). John Wiley and Sons, Inc., New York, pp. 83–110.

Sherman D. M., and Randall S. R. (2003) Surface complexation of arsenic(V) to iron(III) (hydr)oxides: structural mechanism from ab initio molecular geometries and EXAFS spectroscopy. *Geochim. Cosmochim. Acta* **67**, 4223–4230.

Smedley P. L., and Kinniburgh D. G. (2002) A review of the source, behaviour and distribution of arsenic in natural waters. *Appl. Geochem.* **17**, 517–568.

Sun X. H., and Doner H. E. (1996) An investigation of arsenate and arsenite bonding structures on goethite by FTIR. *Soil Sci.* **161**, 865–872.

Tanwar K., Lo C., Eng P. J., Catalano J. G., Walko D. A., Brown, Jr., G. E., Waychunas G. A., Chaka A. M., and Trainor T. P. (2007) Surface diffraction study of the hydrated hematite ($1\bar{1}02$) surface. *Surf. Sci.* **601**, 460–474.

Thirunavukkarasu O. S., Viraraghavan T., and Subramanian K. S. (2003) Arsenic removal from drinking water using iron oxide-coated sand. *Water Air Soil Pollut.* **142**, 95–111.

Trainor T. P., Eng P. J., and Robinson I. K. (2002) Calculation of crystal truncation rod structure factors for arbitrary rational surface terminations. *J. Appl. Crystallogr.* **35**, 696–701.

Venema P., Hiemstra T., and Van Riemsdijk W. H. (1997) Interaction of cadmium with phosphate on goethite. *J. Colloid Interface Sci.* **192**, 94–103.

Walker S. R., Jamieson H. E., Lanzirotti A., Andrade C. F., and Hall G. E. M. (2005) The speciation of arsenic in iron oxides in mine wastes from the Giant gold mine, N.W.T.: Application of synchrotron micro-XRD and micro-XANES at the grain scale. *Can. Mineral.* **43**, 1205–1224.

Waychunas G. A., Rea B. A., Fuller C. C., and Davis J. A. (1993) Surface chemistry of ferrihydrite: Part 1. EXAFS studies of the geometry of coprecipitated and adsorbed arsenate. *Geochim. Cosmochim. Acta* **57**, 2251–2269.

Waychunas G. A., Davis J. A., and Fuller C. C. (1995) Geometry of sorbed arsenate on ferrihydrite and crystalline FeOOH: Reevaluation of EXAFS results and topological factors in predicting sorbate geometry, and evidence for monodentate complexes. *Geochim. Cosmochim. Acta* **59**, 3655–3661.

Waychunas G. A., Fuller C. C., Rea B. A., and Davis J. A. (1996) Wide angle X-ray scattering (WAXS) study of "two-line" ferrihydrite structure: Effect of arsenate sorption and counter-ion variation and comparison with EXAFS results. *Geochim. Cosmochim. Acta* **60**, 1765–1781.

Waychunas G. A., Trainor T. P., Eng P. J., Catalano J. G., Brown, Jr., G. E., Davis J. A., Rogers J. H., and Bargar J. R. (2005a) Surface complexation studied via combined grazing-incidence EXAFS and surface diffraction: arsenate

on hematite (0001) and (10-12). *Anal. Bioanal. Chem.* **383**, 12–27.

Waychunas G. A., Kim C. S., and Banfield J. F. (2005b) Nanoparticulate iron oxide minerals in soils and sediments: unique properties and contaminant scavenging mechanisms. *J. Nanoparticle Res.* **7**, 409–433.

Zhang Z., Fenter P., Cheng L., Sturchio N. C., Bedzyk M. J., Machesky M. L., and Wesolowski D. J. (2004) Model-independent X-ray imaging of adsorbed cations at the crystal-water interface. *Surf. Sci.* **554**, L95–L100.

Associate editor: Roy A. Wogelius